Copyright WILEY-VCH Verlag GmbH & Co. KGaA, 69469 Weinheim, Germany, 2018.

ADVANCED MATERIALS

Supporting Information

for *Adv. Mater.,* DOI: 10.1002/adma.201707077

Nanoparticle Interactions Guided by Shape-Dependent Hydrophobic Forces

*Shu Fen Tan, Sanoj Raj, Geeta Bisht, Harshini V. Annadata, Christian A. Nijhuis, Petr Král, and Utkur Mirsaidov**

Copyright WILEY-VCH Verlag GmbH & Co. KGaA, 69469 Weinheim, Germany, 2017.

Supporting Information

Nanoparticle Interactions Guided by Shape-Dependent Hydrophobic Forces

Shu Fen Tan[1, 2, 3], Sanoj Raj[4], Geeta Bisht[1, 2], Harshini V. Annadata[5], Christian A. Nijhuis[3, 5, 7], Petr Král[4, 6], and Utkur Mirsaidov[1, 2, 3, 7]*

1. Department of Physics, National University of Singapore, 117551, Singapore

2. Centre for BioImaging Sciences and Department of Biological Sciences, National University of Singapore, 117557, Singapore

3. Centre for Advanced 2D Materials and Graphene Research Centre, National University of Singapore, 117546, Singapore

4. Department of Chemistry, University of Illinois at Chicago, Chicago, Illinois 60607, USA

5. Department of Chemistry, National University of Singapore, 117543, Singapore

6. Departments of Physics and Biopharmaceutical Sciences, University of Illinois at Chicago, Chicago, Illinois 60607, USA

7. NUSNNI-NanoCore, National University of Singapore, 117411, Singapore

*Correspondence: mirsaidov@nus.edu.sg

Table of Contents

1. Characterization of CTA^+ capping layers on gold surfaces using X-ray photoelectron spectroscopy (XPS) 2

2. Spacing between nanocubes in the assemblies 3

3. Rotation dynamics of nanocubes during post-attachment re-alignment 4

4. Misaligned attachment of nanocubes 5

5. Attachment modes of nanocubes in a solution observed *in situ* and *ex situ* 6

6. ζ-potential of nanoparticles 8

7. van der Waals and electrostatic interactions between nanoparticles 9

8. *In situ* experiments probing the interaction dynamics between gold nanoparticles at high CTAB concentration 10

9. Atomistic MD simulations of NC-NC and NS-NS interactions 11

10. Water arrangement around the gold nanospheres capped with a monolayer of CTA^+ 14

11. Attachment between the nanoparticles capped with thiolated-polyethylene glycol 14

12. Supporting video captions 16

13. Supporting references 17

1. Characterization of CTA^+ capping layers on gold surfaces using X-ray photoelectron spectroscopy (XPS)

Using XPS, we established that in a 1 mM and 20 mM CTAB solution, a flat gold surface is capped with monolayer and bilayer of CTA^+, respectively.[1, 2] First, we prepared an ultra-smooth (root-mean-square roughness of ~ 5 Å determined by AFM) template-stripped gold[3] substrate by coating a clean Si (100) wafer (with a native SiO_2 layer) with 200-nm thick gold film. Gold was deposited at a rate of 0.7 Å$/s$ and at a base pressure of $\sim 5 \times 10^{-7}$ mbar using a thermal evaporator (ShenYang KeYi, China). Next, clean glass slides were prepared using piranha solution (30% H_2O_2: concentrated H_2SO_4 = 1:3; cleaning time: ~15 min), which were then rinsed thoroughly with deionized water and blow-dried with N_2 gas. These slides were then treated with plasma for 5 minutes under 5 mbar of oxygen. Afterwards, we glued the slides onto the gold coated side of the Si wafer using a thermal adhesive (EPO-TEK 353ND, Epoxy Technology, Inc., Billerica, MA, USA). The glue was cured at 80 °C in an oven (ZRD-A5110A, ZHICHENG, Shanghai, China) for 16 hours. Next, we stripped the gold film from the wafer using a razor blade and immersed this metal/glue/glass template-stripped substrates into the aqueous CTAB solutions for 16 hours.[3, 4]

Next, we rinsed the substrates with a copious amount of deionized water and blow-dried with N_2 gas before proceeding to XPS measurements. We characterized both substrates using an ESCALAB Mark 2 system (Omicron, Taunusstein, Germany) equipped with an Omicron (EA 125 U7) hemispherical electron spectrometer and X-ray source (Omicron Twin Anode X-ray, Mg/Al source). XPS spectra were obtained at a pass energy of 20 eV with full width at half maximum (FWHM) of 1.2 eV. Mg-Kα radiation source at a power of 300 W (15 kV × 20 mA) was used for the measurements. The data were fitted using XPS PEAK software v.4.1 (Raymund Kwok, The Chinese University of Hong Kong, Shatin, Hong Kong).

The XPS spectra in Figure S1A-B show the carbon signals (black circles show the raw peak intensity) for the samples immersed into 1 mM and 20 mM aqueous CTAB solutions. There are five significant carbon signals fitted to the raw data: sp^3C (green solid lines), sp^2C (black solid lines), C-N (brown solid lines), C-O (blue solid lines) and O-C=O (dark blue solid lines). Shirley background was adopted prior to peak fitting.[5, 6] All the curves were fit to a Voigt function with the Lorentzian to Gaussian ratio of 30:70. Among them, only sp^3C and C-N are arising from the surface-bound CTAB, whereas the rest are probably from the adventitious (adv) carbon contaminants[7] during the sample preparation and transfer of the

sample under ambient condition. The contribution from an element i is given by $n_i = I_{i_orb}/S_{i_orb}$ (ref. [8]). Here, I_{i_orb} and S_{i_orb} are the sum of the area under the Voigt profiles and the sensitivity factor of particular orbitals, respectively. In this case, we summed the peak areas from the sp^3C and C-N contributions towards the C_{1s} orbital ($I_{C_{1s}} = I_{sp^3\,C} + I_{C-N}$). $I_{sp^3\,C}$ and I_{C-N} are the areas under the Voigt curves with the peak values at 285.1 eV and 286.2 eV, respectively. The sensitivity factor for the C_{1s} in the spectral region of interest is $S_{C_{1s}} = 0.25$.[8] We obtained the C_{1s} ratio of 1.8 for the gold surfaces treated with 20 mM and 1 mM CTAB. This suggests that at 1 mM and 20 mM CTAB concentrations, CTA^+ forms a monolayer and bilayer on a gold surface, respectively.

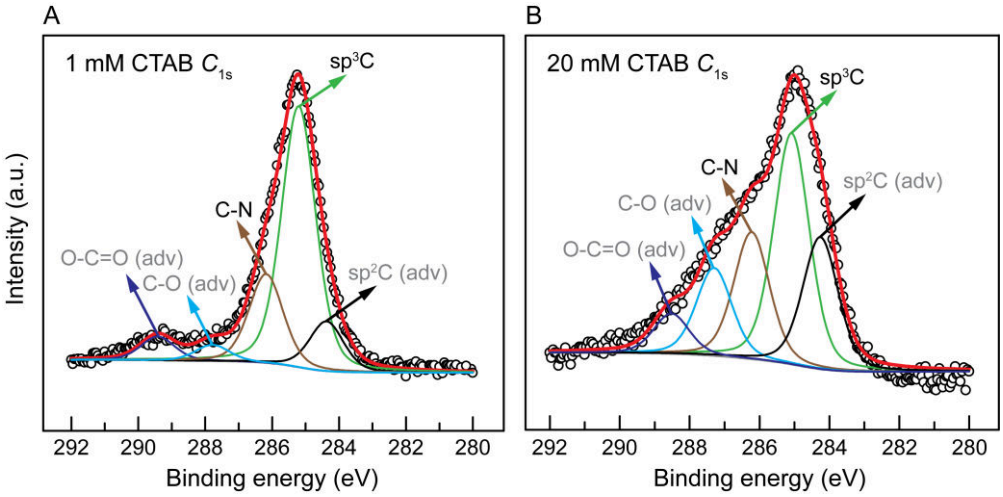


Figure S1. XPS spectra of the C_{1s} regions of the gold surfaces treated with (**A**) 1 mM CTAB and (**B**) 20 mM CTAB.

2. Spacing between nanocubes in the assemblies

Figure S2A-B shows *in situ* and *ex situ* transmission electron microscopy (TEM) images of gold nanocube (NC) assemblies that formed inside the liquid cell and after drop-casting the NC solution (3×10^{13} NCs/mL, $\lesssim$ 1 mM CTAB) onto a carbon film of a TEM grid, respectively. First, recall that the linear chain length of a CTAB polymer is ~2.2 nm (ref.[9]). From our measurements, the average spacing between the neighboring NCs in these assemblies is 1.2 ± 0.3 nm for the *in situ* experiments and 2.8 ± 1.0 nm for the *ex situ* experiments (Figure S2C). We attribute this difference in the pairwise spacings between the *in situ* and *ex situ* results to the difference in packing of the CTA^+ on the surface of the NCs. In the case of *in situ* experiments at $\lesssim$ 1 mM CTAB concentration, CTA^+ forms a monolayer on the surface of the NCs, and these monolayers are interdigitated and compressed upon the attachment of the NCs.

For the *ex situ* experiments, CTAB concentration increases when water starts to dry on a TEM grid, and multilayers of CTA^+ can form on the surface of NCs.[9] The large NC-NC spacing in our *ex situ* observations (*i.e.*, spacing between the NCs in *ex situ* assemblies is ~2-3 times larger than in the *in situ* case) is probably caused by the presence of these surfactant multilayers.[9]

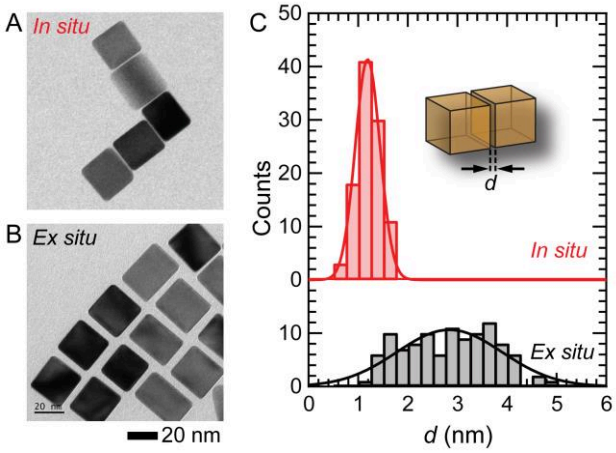


Figure S2. TEM images of gold NC assemblies observed (**A**) *in situ* (inside the liquid cell) and (**B**) *ex situ* (drop-casted and dried on a carbon grid), respectively. (**C**) The distributions of pairwise separations between the neighboring gold NCs measured in the assemblies formed *in situ* (red) and *ex situ* (black). The smooth curves represent the Gaussian fits centered at 1.2 ± 0.3 nm (*in situ*) and 2.8 ± 1.0 nm (*ex situ*) for these distributions.

3. Rotation dynamics of nanocubes during post-attachment re-alignment

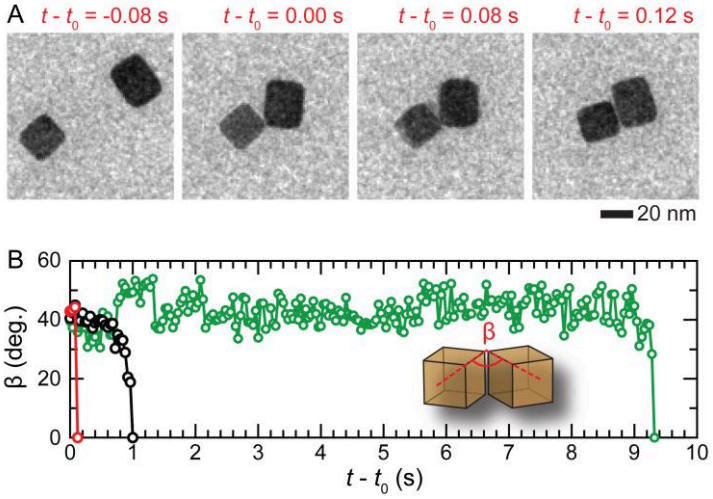


Figure S3. (**A**) A time series of TEM images showing an example of a post-attachment alignment event. Here, t_0 represents the time point at which two NCs come into contact. (**B**) The angle between the two NCs undergoing post-attachment alignment shown in (A), Figure 2B, and Figure 3A (TEM image series in the fourth row) are plotted by red, black, and green circles, respectively.

The detailed analysis of post-attachment alignment events revealed that the alignment part of the entire attachment process is fast ($\lesssim$ 0.5 s) (Figure S3A, t_0 = 0.08 s – 0.12 s).

However, the alignment does not always occur immediately after the attachment; it may take few seconds before the NCs start rotating into an aligned attachment configuration (black and green data points in Figure S3B).

4. Misaligned attachment of nanocubes

In addition to the aligned face-to-face attachment modes discussed in the manuscript (Figure 2), we also observed that the NCs might undergo attachment where the final assembly configuration is misaligned (*i.e.,* the attachment between the NCs in a final assembly is not in a face-to-face configuration). Figure S4 shows the two possible misaligned attachment modes observed in our study: 1) edge-to-edge attachment (Figure S4A) and 2) edge-to-face attachment (Figure S4B). In both cases, after the NCs come into contact, they are stuck permanently (*i.e.,* within our observation time of ~1 min), and these NCs no longer rotate into an aligned face-to-face attachment configuration.

The reason for this failed alignment is gold-gold bonding between the crystalline NCs during their contact. The affinity of CTA^+ to {110} gold planes at the edge of the NCs is lower than to {100} face facets. This low capping density at the NC edges makes the NC prone to bonding with the gold face or edge of another NC upon attachment. The gold-gold bonding between the NCs can be clearly seen when the spacing between the gold NCs in the misaligned attachments in Figure S5 is compared with the aligned attachments in Figure S2A-B. However, the attachment events that result in permanently misaligned attachment configurations are less frequent than the aligned face-to-face attachment events (SI Section 5).

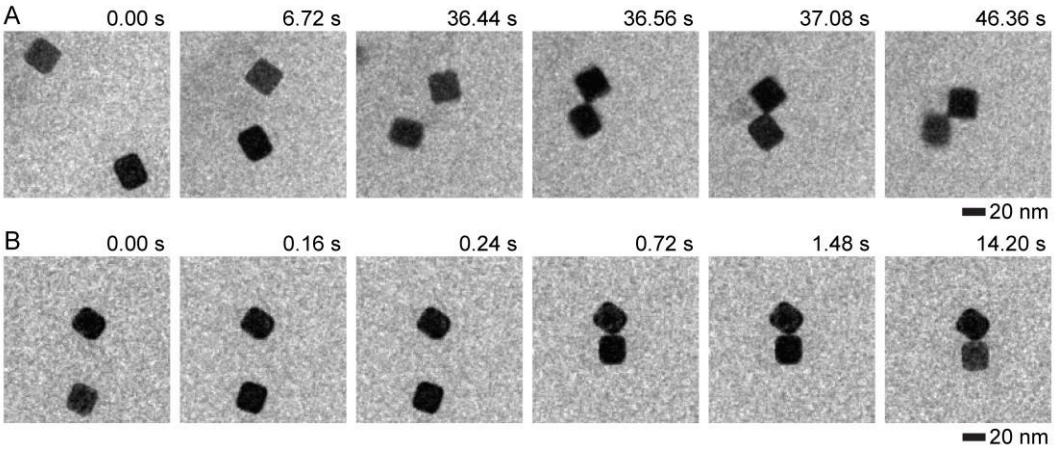


Figure S4. A time series of TEM images of gold NC assemblies displaying two modes of misaligned attachment: (**A**) edge-to-edge and (**B**) face-to-edge attachments.

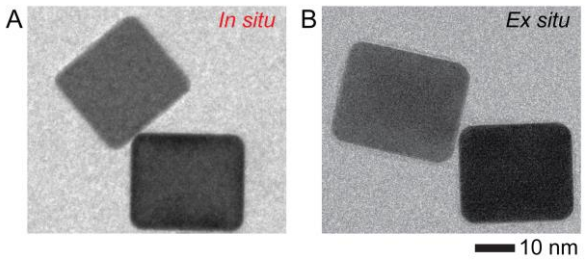


Figure S5. TEM images of misaligned attachments between two gold NCs observed (**A**) *in situ* (inside the liquid cell) and (**B**) *ex situ* (drop-casted and dried on a carbon grid), respectively.

5. Attachment modes of nanocubes in a solution observed *in situ* and *ex situ*

Figure S6 summarizes the frequency of all NC-NC attachment modes observed in our *in situ* liquid cell TEM imaging experiments. The likelihood for NCs to undergo aligned face-to-face attachment either *via* prealigned attachment (~57%) or post-attachment alignment (~18%) is 75%. The edge-to-edge and edge-to-face misaligned attachment modes shown in Figure S4 occur in ~9% and ~16% of the attachment events, respectively (Figure S6).

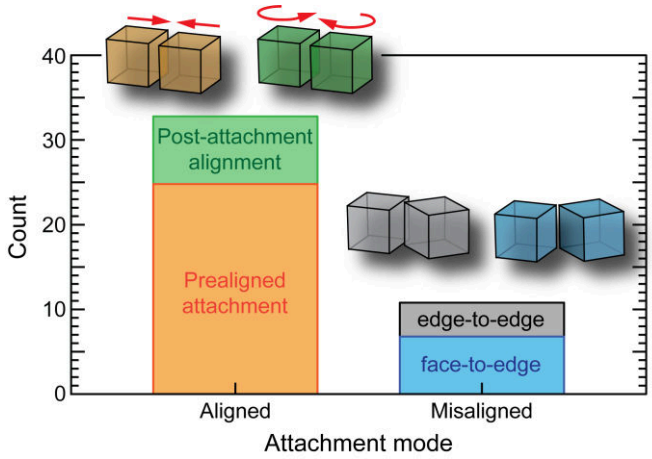


Figure S6. The number of different NC-attachment modes observed during the *in situ* TEM experiments. The total number of the attachment events is 44.

Furthermore, we compared the different attachment modes observed *in situ* with the *ex situ* experiments. Figure S7A shows the representative TEM images of gold NC-dimers observed *ex situ*, where we drop-casted the ~3 μL of NC solution ($\lesssim$ 1 mM CTAB, 3×10^{13} NCs/mL) onto a carbon film of a TEM grid. Here, the assemblies also can be classified into two attachment mode groups (Figure S7B) – aligned and misaligned attachments. In the case of aligned attachments, we find that most of the NCs attach in a parallel face-to-face configuration, and only in few cases, the faces between the NCs display slight asymmetric gap (slight misalignment). In the case of misaligned attachments, we find the NCs in a face-to-edge

attachment configuration. Note that these *ex situ* NC assemblies are driven by capillary forces that arise during the drying of water on a TEM grid, which results in the assemblies of close-packed NCs, as found in earlier studies.[9-13] Here, the low frequency of misaligned attachment events is due to the effect of this drying-induced capillary force, which drives the misaligned NCs into the aligned configuration.[9] Moreover, as a result of these capillary forces, any NC-dimer in the edge-to-edge misaligned configuration is expected to experience a larger aligning capillary torque than the dimers in the face-to-edge configuration, which explains the absence of the edge-to-edge misaligned attachment events in our *ex situ* results. Nevertheless, the most favorable attachment mode for these CTA^+-capped NCs is the aligned face-to-face attachment configuration as observed both in our *in situ* and *ex situ* experiments.

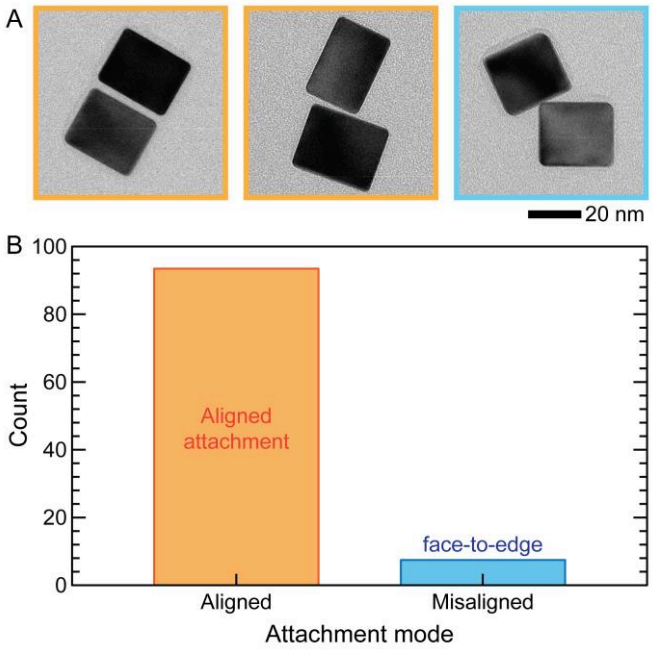


Figure S7. (**A**) TEM images of perfectly aligned attachment, aligned attachment with a slight asymmetric gap, and misaligned face-to-edge attachment configurations for *ex situ* experiments. These samples were prepared by drop-casting a NC solution on a carbon film of a TEM grid. (**B**) The number of different NC-attachment modes for 102 attachment events. These *ex situ* assemblies are subject to capillary forces because the carbon film of a TEM grid needs to be dried prior to imaging.

6. ζ-potential of nanoparticles

To understand the effect of the charge of the gold nanoparticles (NPs) on their assembly, we measured ξ-potential for NPs with different shapes solvated in solutions (water+CTAB). Figure S8 shows the ξ-potential measurements fitted using Smoluchowski model[14] for NPs in a solution: NCs, nanobipyramids (NBPs), nanorods (NRs), nanospheres (NSs) before (~20 mM CTAB) and after ($\lesssim$ 1 mM CTAB) washing treatment. Overall, the washed NPs had lower ξ-potential in comparison to the unwashed NPs. We believe that the unwashed NPs have a larger amount of CTA^+ (hence their higher surface charge), which causes them to repel each other and prevent the contact and the subsequent attachment (SI Section 8).

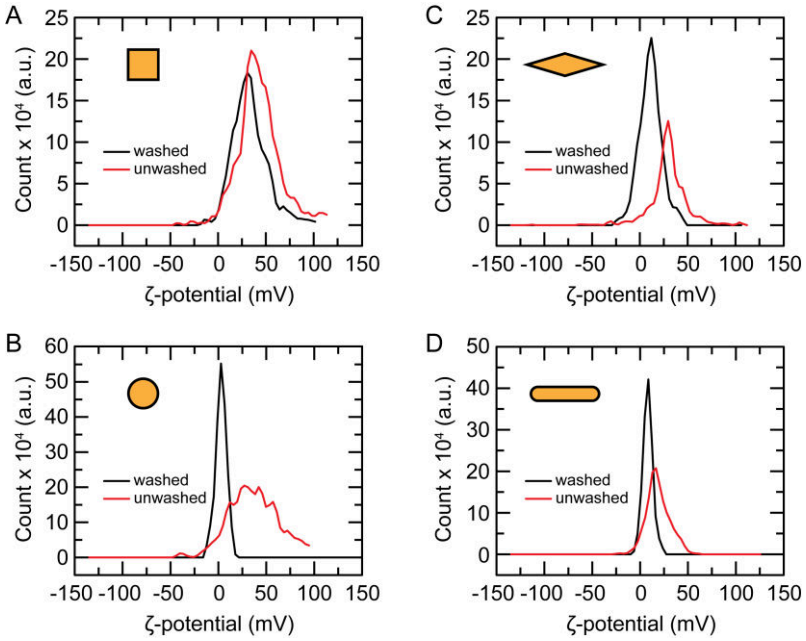


Figure S8. Fitted ξ-potential for gold NPs of different shapes: (**A**) NCs, (**B**) NSs, (**C**) NBPs and (**D**) NRs for two different conditions: before (solid black lines) and after (solid red lines) washing treatment.

Nanoparticles	ξ-potential before washing treatment (mV)	ξ-potential after washing treatment (mV)
Nanocubes	32.1	10.2
Nanospheres	40.3	2.0
Nanorods	38.0	6.8
Nanobipyramids	35.4	8.2

Table S1. Summary of Figure S8: The average ξ-potential values of different-shape gold NPs in solutions before and after washing treatment.

7. van der Waals and electrostatic interactions between nanoparticles

To qualitatively test whether an attractive vdW force between the gold cores of the NPs alone is sufficient enough to result in NP attachment, we calculated the net interaction energy between the NPs as a function of the distance. Here, we only accounted for the vdW attraction and electrostatic repulsion between the NPs capped with a monolayer and bilayer of CTA^+ in $\lesssim$ 1 mM and ~20 mM ionic solutions, respectively (SI Section 1). From our MD simulations (SI Section 9), the equilibrium surface charge is +40*e* and +35*e* for NCs (side-length of 5.3 nm) and NSs (diameter of 5.3 nm) capped with a monolayer of CTA^+, respectively. Since the Debye screening length is large (*i.e.,* ~10 nm and ~5 nm for $\lesssim$ 1 mM and ~20 mM solution, respectively), for simplicity, we ignored the charge screening of the nanoparticles. For simplicity, we also assumed the particles to be spherical when estimating the electrostatic interactions between them. The total interaction energy between two NCs is then the sum of the electrostatic repulsion and vdW[15] attraction:

$$U_{\text{tot}}(D) = U_{\text{el}}(D) + U_{\text{vdW}}(D) = \frac{(ze)^2}{4\pi\varepsilon_0\varepsilon(D+a)} - \frac{A\,a^2}{12\pi}\left[\frac{1}{D^2} - \frac{2}{(D+a)^2} + \frac{1}{(D+2a)^2}\right].$$

Here, ze = +40*e* is the net equilibrium charge of the NC obtained from the MD simulations (SI Section 9), $1/\kappa$ = 9.6 nm – Debye length, ε_0 = 8.85×10^{-12} F m^{-1} – permittivity of free space, ε = 80 – relative permittivity of water, a = 5.3 nm – the side length of the gold NC, A = 3×10^{-19} J – the Hamaker constant for gold-gold interaction in water, and D – the separation between the faces of two gold NCs.

Similarly, in the case of two interacting spherical NPs with radius R, we obtain:[16]

$$U_{\text{tot}}(D) = U_{\text{el}}(D) + U_{\text{vdW}}(D) = \frac{(ze)^2}{4\pi\varepsilon_0\varepsilon(D+2R)} - \frac{A}{12}\left(\frac{R}{D\left(1+\frac{D}{4R}\right)} + \frac{1}{\left(1+\frac{D}{2R}\right)^2} + 2ln\,\frac{D\left(1+\frac{D}{4R}\right)}{R\left(1+\frac{D}{2R}\right)^2}\right).$$

Figure S9 displays the plots of the interaction energies for two NCs and two NSs. These plots show that an electrostatic barrier in each case is significant. Moreover, this energy barrier is 10 times larger for the NPs capped with the CTA^+ bilayer than for NPs with CTA^+ monolayer. Therefore, in the presence of the hydrophobic forces acting between the NPs, the lowering of the energy barrier can bring into contact the NPs capped with CTA^+ monolayer and not CTA^+ bilayer. Our MD simulations support this assertion (SI Section 9).

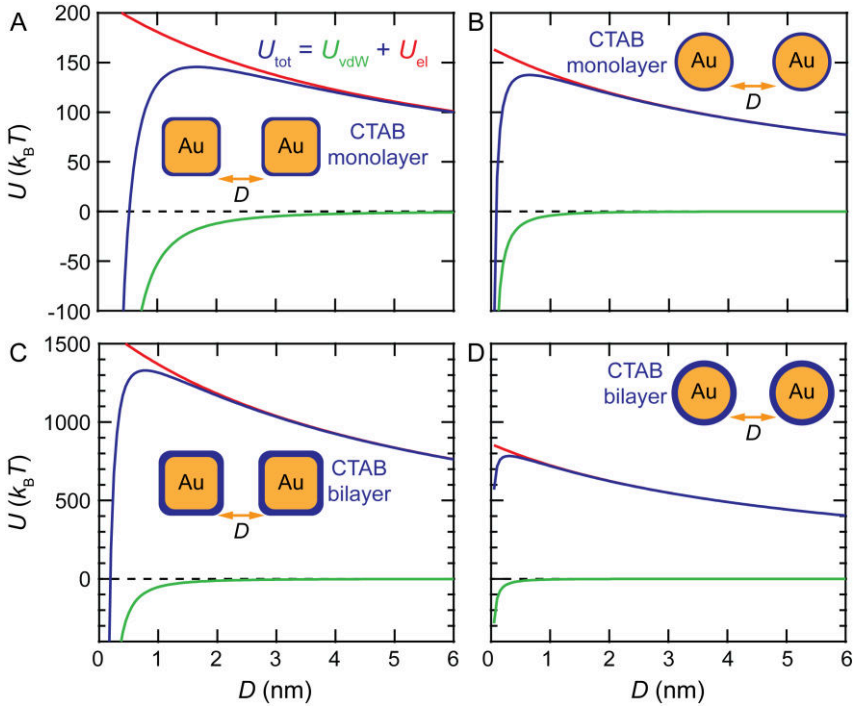


Figure S9. Calculated strength of the electrostatic, vdW, and total interactions between (**A**) two NCs and (**B**) two NSs, each capped with a monolayer of CTA^+. Calculated strength of the electrostatic, vdW, and total interactions between (**C**) two NCs and (**D**) two NSs, each capped with a bilayer of CTA^+.

8. *In situ* experiments probing the interaction dynamics between gold nanoparticles at high CTAB concentration

Figure S10 shows the dynamics of NPs in ~20 mM aqueous CTAB solution. We believe that this excess of CTAB in the solution promotes formation of micellar structures and a capping CTA^+ bilayer on the surface of the NPs.[17] The increased amount of CTA^+ on the NPs increases the charge of the NPs as confirmed by the ζ-potential measurements (SI Section 6). Therefore, these NPs do not attach regardless of their shape because of the electrostatic repulsion between them. However, when these NPs undergo washing treatment, which reduces the CTAB concentration in solution to $\lesssim$ 1 mM, the amount of CTA^+ on the surface of the NPs and their charges decrease; in this case, NPs undergo contact and can attach when the binding strength due to hydrophobic forces is large enough (Figure 3).

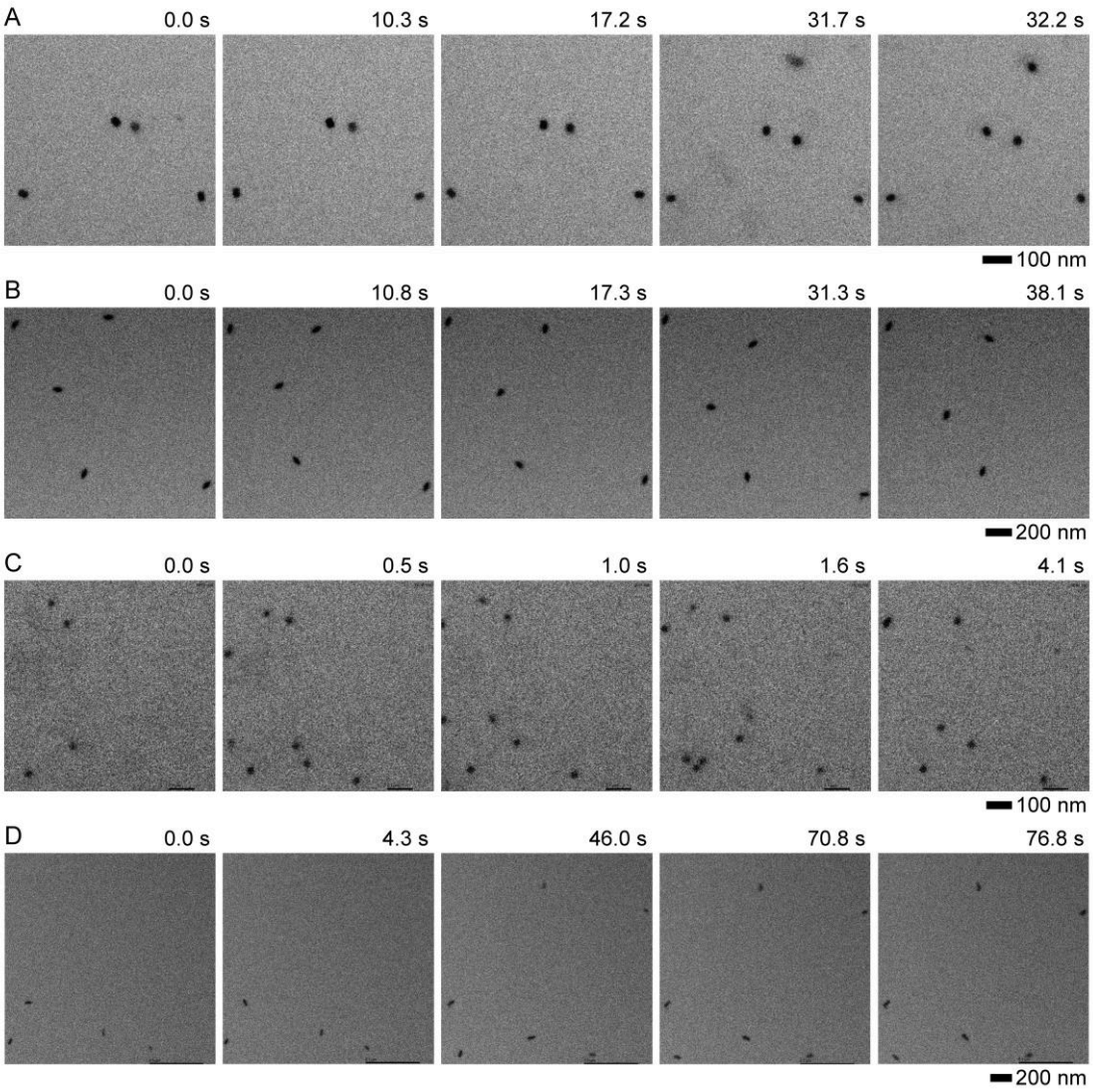


Figure S10. A time series of TEM images showing that gold (**A**) NCs, (**B**) NBPs, (**C**) NSs and (**D**) NRs do not attach in a ~20 mM aqueous CTAB solution. NPs are electrostatically stabilized by the excess amount of CTA^+ capping them.

9. Atomistic MD simulations of NC-NC and NS-NS interactions

To understand the impact of different interactions during the attachment of NPs, we performed atomistic MD simulations, where we separately switched on and off the vdW interaction between the NP cores and changed the number of ligands on NPs.

Figure S11A shows the dynamics of two interacting NCs both in the absence and presence of gold-gold vdW interaction between their gold cores. We found that NCs attract (*i.e.,* approach) even when the gold-gold vdW attraction is absent (*i.e.*, the gold-gold vdW interaction between the NCs is set to 0). This attraction between NCs in the absence of vdW interaction indicates that another attractive force is acting between the NCs during their

assembly. Our analysis revealed that this attractive force is a hydrophobic force and is due to partly hydrophobic CTA^+ ligands capping the NCs (see the main text).

In the case of NSs, once the vdW attraction between the NS gold cores is turned off (Figure S11B), the NSs move apart because of the electrostatic repulsion. The net equilibrium surface charges of the NC and NS capped with a CTA^+ monolayer are approximately +40*e* and +35*e*, respectively. The attractive hydrophobic interaction alone is not sufficient to bring the NSs close by for the attachment to take place. Therefore, the vdW attraction between their gold cores is essential for the attachment of the NSs.

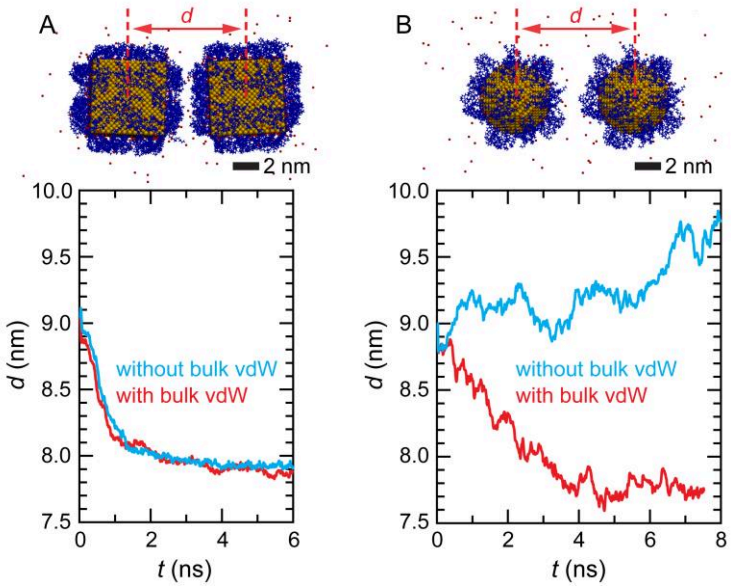


Figure S11. (**A**) Center-to-center distance obtained from MD simulation of two interacting NCs capped with a CTA^+ monolayer. Blue and red curves represent the spacing between the NCs in the absence and presence of the vdW coupling between their gold cores. NPs approach each other and undergo attachment in both cases. This suggests that hydrophobic force between the NCs alone can drive their attachment regardless of their surface charges because of the surfactant. (**B**) The center-to-center distance between two interacting NSs increases in the absence of vdW attraction between the gold cores and decreases when the vdW attraction is present. This suggests that hydrophobic interaction alone is not sufficient to overcome the electrostatic repulsion between the NSs, and vdW force between the gold NSs is needed to provide an additional attraction for NSs to come together and attach.

To test the effect of the amount of capping agent on the NP surface, we also examined the interaction between the NPs capped with a bilayer of CTA^+. For this case, the MD simulations revealed that the net NC-NC and NS-NS interactions are repulsive and the NPs move apart (Figure S12). Note that the gold-gold vdW interaction between the NPs is included for both the NCs and NSs. The origin of this repulsion is purely electrostatic since the net equilibrium charge for NCs and NSs capped with the CTA^+ bilayer obtained from MD simulations is approximately +110*e* and +80*e*, respectively.

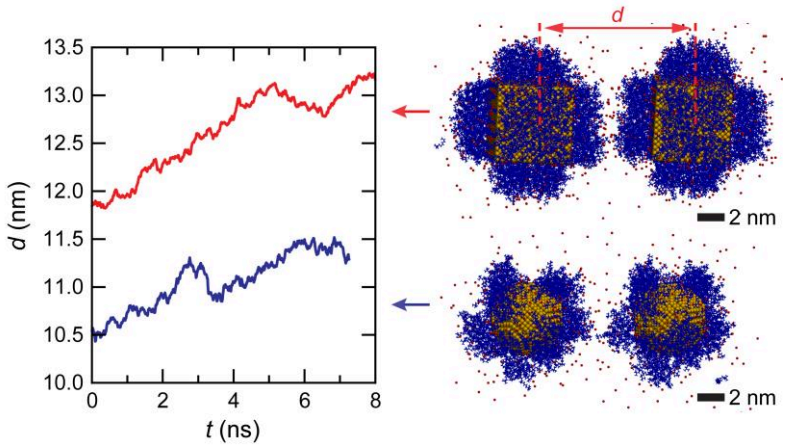


Figure S12. Center-to-center distance between two interacting CTAB bilayer capped NCs (red curve) and two NSs (blue curve) obtained from MD simulations. In both cases, NPs move apart.

To further validate that the repulsion between NPs is modulated by the amount of NP bound CTA^+ ligands and the subsequent charging of the NPs, we re-plotted the center-to-center distance between two NCs with monolayer and bilayer of CTA^+ (Figure S11A and S12) along with the distance between the NCs with 1.5 CTA^+ layers. Our comparisons show that NCs approach each other only when they are capped by a monolayer of CTA^+ (Figure S13). In the case of bilayer CTA^+-capped NCs, NCs move apart faster than the NCs with 1.5 layers of CTA^+ indicating that the electrostatic repulsion is driving the NCs apart.

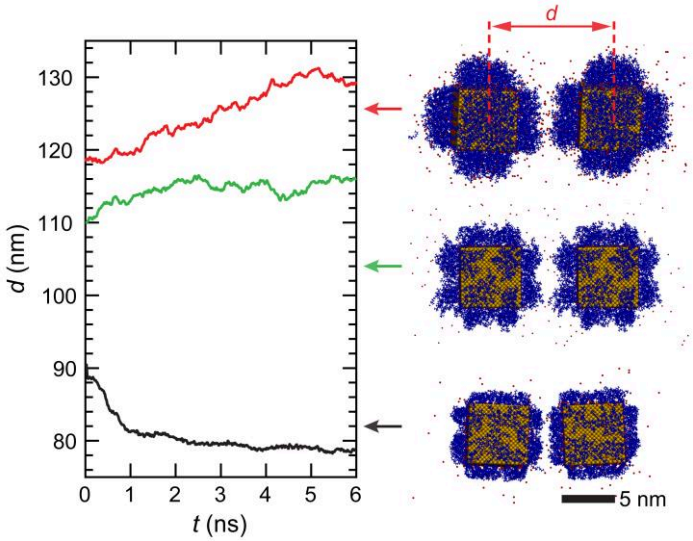


Figure S13. Center-to-center distance between two interacting NCs capped with monolayer (black), 1.5-layer (green), and bilayer (red curve) of CTA^+. The attraction between the NCs is observed only for the NCs with the CTA^+ monolayer capping. The respective net equilibrium charges for the NCs with the monolayer, 1.5-layer, and bilayer CTA^+ are +40*e*, +70*e*, +110*e*.

10. Water arrangement around the gold nanospheres capped with a monolayer of CTA^+

To understand how water behaves near the hydrophobic NPs capped with a monolayer of CTA^+, and how the hydrophobic interaction aids in the attachment of NPs, we have studied the arrangement of water molecules around the NPs' CTA^+ ligands. We found that the first and second water layers are at 2.8 Å and 5.6 Å away from the CTA^+ ligands, respectively (Figure S14A-B, Figure 2E). The water density in these water layers is higher than in bulk water, while the average number of H-bonds per water molecules is lower (Figure 2E).

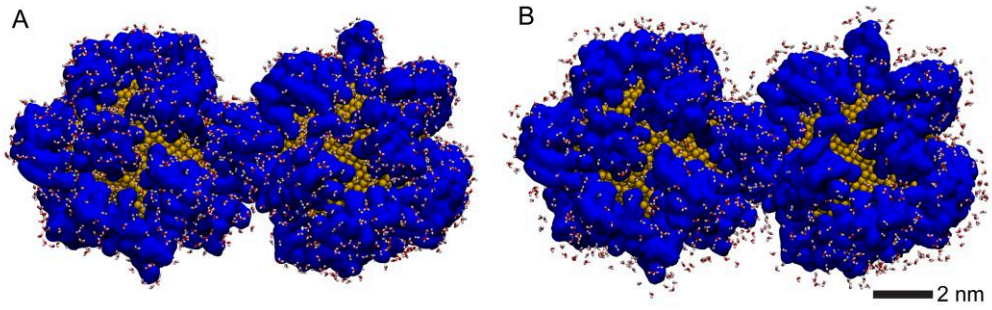


Figure S14. Arrangement of water molecules at a distance of (**A**) 2.8 Å and (**B**) 5.6 Å from the CTA^+ ligands. The blue isosurfaces represent the CTA^+ ligands, and the yellow balls represent the gold atoms of the NSs. Water molecules are shown in licorice representation.

11. Attachment between the nanoparticles capped with thiolated-polyethylene glycol

To test the effect of hydrophobicity on the NP attachment, we also studied the interaction dynamics between the gold NCs and between the gold NSs, both capped with thiolated-polyethylene glycol (PEG-SH) (CH_3-$(OCH_2CH_2)_9$-SH) (Figure S15A). These NPs with PEG capping were obtained from our CTA^+-capped gold NCs and NSs through a ligand exchange reaction. Briefly, 1.0 mL of CTA^+-capped gold NCs (at a concentration of 3×10^{12} NC/mL) and NSs (at a concentration of 2×10^{12} NS/mL) were first centrifuged twice and re-dispersed in 0.2 mL of a 20 mM aqueous PEG-SH solution for 1 hour at room temperature. PEG-SH has thiol moiety can displace CTA^+ of the gold NPs (binding energy of CTA^+ on {111} gold plane:[18] ~109 kJ/mol or ~44 k_BT) because of the formation of a strong Au-S thiolated bond[19] (~209 kJ/mol or ~84 k_BT). The NPs were washed and re-dispersed in deionized water before loading into the liquid cell for *in situ* TEM experiments.

Similar to our observations reported in Figure 3 of the main text, these *in situ* TEM experiments show that the pairwise interactions between the PEG-capped gold NPs can either result in permanent attachments (Figure S15B) or post-attachment detachments (transient attachments) (Figure S15C). Figure S15D shows the frequency of permanent attachments and

post-attachment detachment events for PEG-capped NCs and NSs. All the pairwise contact events (total of 19) between the NCs resulted in permanent attachments (100%), whereas only ~67% of the contacts between the NSs formed permanent attachments. Note that the attachment frequency for CTA^+-capped NCs and the NSs are ~84% and ~52%, respectively (Figure 3C).

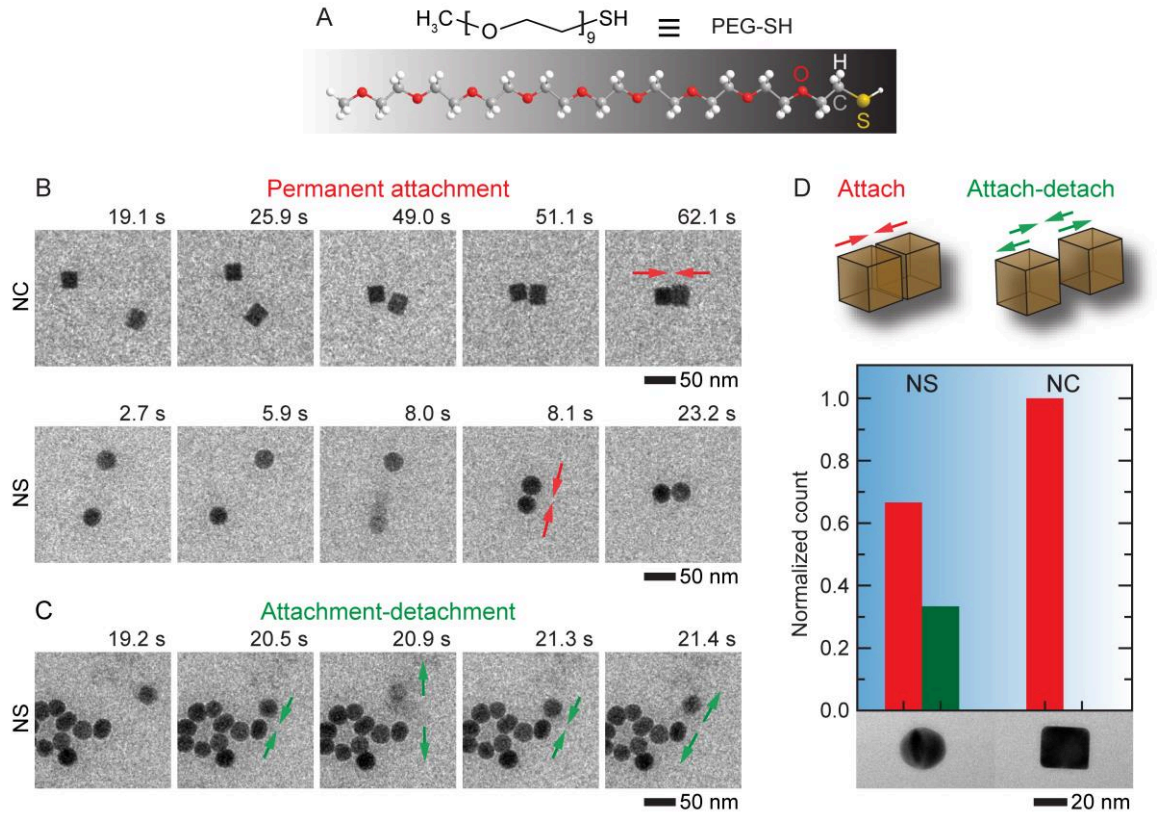


Figure S15. Interaction between PEG-capped gold NPs. (**A**) The chemical structure of PEG-SH surfactant based on a ball-and-stick model. (**B**) A time series of TEM images showing the permanent attachments (red arrows) between two NCs and two NSs. (**C**) A sequence of TEM images showing the transient attachments between two NSs (*i.e.*, NS-NS attachment followed by their detachment) (green arrows). (**D**) Frequency of the permanent (red) and transient (green) attachment events for the NSs and NCs. The total number of the events for the NSs and NCs are 51 and 19, respectively.

12. Supporting video captions

Video 1: Face-to-face attachment of two CTA^+-capped gold nanocubes into a NC-dimer in water.

Video 2: Face-to-face attachment of three CTA^+-capped gold nanocubes into a linear trimer in water.

Video 3: Face-to-face attachment of three CTA^+-capped gold nanocubes into an L-shaped trimer in water.

Video 4: Assembly of a small NC-array from one NC-trimer and two nanocube-dimer blocks.

Video 5: Face-to-face attachment of two CTA^+-capped gold NCs into a nanocube-dimer *via* prealigned attachment pathway.

Video 6: Face-to-face attachment of two CTA^+-capped gold NCs into a nanocube-dimer *via* post-attachment alignment pathway.

Video 7: MD simulation showing the face-to-face attachment of two gold nanocubes capped with CTA^+ monolayer into a nanocube-dimer *via* prealigned attachment pathway in water.

Video 8: MD simulation showing the face-to-face attachment of two gold nanocubes capped with CTA^+ monolayer into a nanocube-dimer *via* post-attachment alignment pathway in water.

Video 9: MD simulation showing the attachment of two gold nanospheres capped with CTA^+ monolayer into a nanosphere-dimer *via* post-attachment alignment pathway in water.

13. Supporting references

[1] I. Gouzman, M. Dubey, M. D. Carolus, J. Schwartz, S. L. Bernasek, *Surf. Sci.* **2006**, *600*, 773.
[2] T. L. Freeman, S. D. Evans, A. Ulman, *Langmuir* **1995**, *11*, 4411.
[3] L. Yuan, L. Jiang, B. Zhang, C. A. Nijhuis, *Angew. Chem.* **2014**, *126*, 3445.
[4] L. Jiang, T. Wang, C. A. Nijhuis, *Thin Solid Films* **2015**, *593*, 26.
[5] J. E. Castle, *Surf. Interface Anal.* **1984**, *6*, 302.
[6] J. Végh, *J. Electron Spectrosc. Relat. Phenom.* **2006**, *151*, 159.
[7] D. J. Miller, M. C. Biesinger, N. S. McIntyre, *Surf. Interface Anal.* **2002**, *33*, 299.
[8] C. D. Wagner, L. E. Davis, M. V. Zeller, J. A. Taylor, R. H. Raymond, L. H. Gale, *Surf. Interface Anal.* **1981**, *3*, 211.
[9] T. K. Sau, C. J. Murphy, *Langmuir* **2005**, *21*, 2923.
[10] G. M. Whitesides, M. Boncheva, *Proc. Natl. Acad. Sci.* **2002**, *99*, 4769.
[11] T. Ming, X. Kou, H. Chen, T. Wang, H. L. Tam, K. W. Cheah, J. Y. Chen, J. Wang, *Angew. Chem.* **2008**, *120*, 9831.
[12] N. R. Jana, *Angew. Chem. Int. Ed.* **2004**, *43*, 1536.
[13] B. Nikoobakht, Z. L. Wang, M. A. El-Sayed, *J. Phys. Chem. B* **2000**, *104*, 8635.
[14] R. J. Hunter, *Zeta potential in colloid science : principles and applications*, Academic Press, London; New York **1981**.
[15] V. Parsegian, *Van Der Waals Forces: a Handbook for Biologists, Chemists, Engineers, and Physicists*, **2005**.
[16] J. N. Israelachvili, *Intermolecular and Surface Forces (Third Edition)*, Academic Press, San Diego **2011**, 253.
[17] S. K. Meena, M. Sulpizi, *Langmuir* **2013**, *29*, 14954.
[18] J. Feng, R. B. Pandey, R. J. Berry, B. L. Farmer, R. R. Naik, H. Heinz, *Soft Matter* **2011**, *7*, 2113.
[19] J. C. Love, L. A. Estroff, J. K. Kriebel, R. G. Nuzzo, G. M. Whitesides, *Chem. Rev.* **2005**, *105*, 1103.